

Advanced Online Broadband Impedance Spectrum Acquisition of Fuel Cells by S-Transform

Hao Yuan[✉], Runben Du, Xueyuan Wang[✉], Xuezhe Wei, and Haifeng Dai[✉], *Senior Member, IEEE*

Abstract—Electrochemical impedance spectrum (EIS) applied in fuel cell characterization and diagnosis facilitates its system management in the vehicular application, but the first consideration of impedance-based management is how to obtain impedance online. The traditional laboratory method based on sine sweep is unsuitable for vehicular EIS measurement as limited by measured time and equipment price. In this article, we design an excitation device that can generate the square wave signal containing many harmonics as the excitation current. Besides, introduce S-transform (ST) for online broadband fuel cell impedance spectrum fast calculation, whose window width can be adaptively changed with frequency, and meanwhile, preserving high computational efficiency by fast Fourier transform operation. Based on this, the performance of ST and the previous method based on Morlet wavelet transform (MWT) is compared under different operating conditions. Extensive experimental results show that the ST can calculate impedance with the mean relative error of less than 3% based on appropriate excitation, while the computed time can be saved by nearly 95% as compared to MWT. Furthermore, the effectiveness and robustness of ST against different current densities, cell temperatures, fault scenarios with various fault degrees, and stable time are also verified through experimentation.

Index Terms—Electrochemical impedance spectrum (EIS), fuel cell, S-transform (ST).

I. INTRODUCTION

HYDROGEN energy development has emerged as a viable pathway for the carbon peak and carbon neutrality [1]. Among different fuel cells, the proton exchange membrane (PEM) fuel cells are now the leading candidate for use due

Manuscript received 6 December 2021; revised 17 February 2022, 29 March 2022, and 15 April 2022; accepted 14 May 2022. Date of publication 1 June 2022; date of current version 12 December 2022. This work was supported in part the National Natural Science Foundation of China under Grant U20A20310. (Corresponding authors: Xueyuan Wang; Haifeng Dai.)

Hao Yuan, Runben Du, Xuezhe Wei, and Haifeng Dai are with the Clean Energy Automotive Engineering Center, Tongji University, Shanghai 201804, China (e-mail: yuanhao@tongji.edu.cn; runbendu@tongji.edu.cn; weixzh@tongji.edu.cn; tongjidai@tongji.edu.cn).

Xueyuan Wang is with the Department of Control Science and Engineering, Tongji University, Shanghai 201804, China (e-mail: Twangxueyuan@tongji.edu.cn).

Color versions of one or more figures in this article are available at <https://doi.org/10.1109/TIE.2022.3177814>.

Digital Object Identifier 10.1109/TIE.2022.3177814

to fast starting, good dynamic response, and low operating temperature [2]. However, the large-scale commercial applications respecting fuel cell vehicles are still limited by durability and environmental adaptability. Therein, it is inevitable to develop advanced fuel cell management systems to improve its performance and service life. But this forms great challenges, since internal states coupled with sophisticated electrochemical processes are implicit and unmeasurable directly with traditional vehicle-used sensors due to the enclosed construction [3], [4]. In this regard, developing the online internal state diagnosis tool is great of significance for fuel cell health management.

The electrochemical impedance spectroscopy (EIS) is a widespread noninvasive technology to study internal dynamics in the frequency domain, which is now being actively applied for the PEM fuel cell [5], [6]. Thanks to the powerful separating capability of the EIS, on the one hand, the effects of operating conditions on internal dynamics can be investigated to evaluate fuel cell output performance [7] [8]. For another, the sensitivity of operating conditions to internal dynamics can also be analyzed by impedance to determine the optimal working boundary [9]. Besides, impedance-based fault diagnosis tools can be developed with the aid of the strong coupling between internal dynamics and characteristic frequencies. For instance, the high-frequency resistance reflecting proton transfer [10], and the low-frequency (LF) capacitance loops or arcs for concentration polarization caused by oxygen diffusion [11], even the LF inductive loops occasioned by humidity dependent ionomer properties [12], contribute to internal water management to avoid or mitigate membrane drying and flooding. The specific LF information indicating oxygen transfer and storage in the catalyst layer can also guide for air starvation diagnosis [13]. Furthermore, the EIS provides a deeper insight into the degradation process of a PEM fuel cell exposed to an accelerated stress experiment [14] and can be used as a compelling symbol to judge its state of health [15]. Hence, the electrochemical impedance is considered as an efficient signal for internal state assessment.

Before using impedance to diagnose or control the PEM fuel cell, the first consideration is how to obtain impedance online. To date, the most commonly used impedance measurement method in the laboratory is to inject sinusoidal signals of different frequencies into the fuel cell in turn by an electrochemical workstation. Nevertheless, this laboratory method is not suitable for actual vehicular fuel cell systems because of measured time, equipment price, and environmental interference [16]. For this,

some online EIS acquisition schemes have been proposed in the literature, which can be generally categorized into two groups, i.e., online estimation and online measurement. The equivalent circuit model (ECM) consisting of resistors and capacitors can be roughly identified for polarization loss judgment based on transient voltage and current with the least-squares technique [17], [18], but such a simplified model is difficult to describe the time-frequency domain characteristics of fuel cells accurately. Overly complex models, such as process impedance model [19] and dimensional impedance model [12], are impossible for online identification.

Compared with the estimation by impedance model, the excitation injection and signal processing-based measurement often yield satisfactory performance. T. Mirai [20] has already integrated an excitation device in the dc/dc converter for 300 Hz impedance measurement to detect hydration state. A similar scheme was also adopted by Hong *et al.* [21] to detect the membrane water content, in which 320 Hz was selected as the characteristic frequency, because the value of this frequency impedance is similar to that of 1 kHz, and meanwhile this frequency is a satisfactory tradeoff between the measurement accuracy of impedance and the capability and cost of hardware. However, obtaining a broadband impedance spectrum is required by sweeping frequency [22], [23], other than hardware limit, and it is also inappropriate for fault diagnosis based on the quantitative polarization loss on account of a long-measured time [24].

To further improve the frequency range and efficiency of impedance spectrum measurement, some researchers have utilized signals with rich harmonic components to stimulate fuel cells. Bulecks *et al.* [25] measured the impedance spectrum using the short-time Fourier transform (SFT) with Chirp signal as disturbance and found it to be orders of magnitude faster than the standard EIS measurement, but their method was only validated by predefined fuel cell models. Katayama and Kogoshi [26] stimulated the fuel cell with multiple sinusoidal waves generated by a multiport bidirectional dc/dc and calculated impedance by fast Fourier transform (FFT). However, the significant shortcoming of the traditional Fourier transform is the lack of time domain information [27], while wavelet transform can realize time subdivision at high frequency and frequency subdivision at the LF of the signal, has attracted great interest in PEM fuel cell impedance calculation. Rubio *et al.* [28] compared the impedance-based fault diagnosis of Fourier transform and wavelet transform, and found that the wavelet transform has higher sensitivity to the change of fuel cell working conditions. Debenjak *et al.* [29] calculated the EIS by utilizing pseudorandom binary sequence and continuous wavelet transform. Similarly, Lu *et al.* [24] also analyzed the time domain of pseudorandom sequence by wavelet transform. Then, final EIS of the PEM fuel cell was determined by maximum likelihood estimation, whereas convolution operation is required at each moment of the original signal, undoubtedly resulting in harsh computational and storage requirements. Hence, Du *et al.* [16] further selected a periodic square wave as excitation current and calculated the fuel cell EIS by Morlet wavelet transform (MWT), where convolution operation is only performed at several

jump moments, significantly decreasing the computational cost. Jin *et al.* [30] also used the complex wavelet transform to simulate the impedance spectrum of the PEM fuel cell under the square excitation, and obtained impedance is very close to the model theoretical value.

Although previous studies have investigated advanced methods respecting online impedance calculation of PEM fuel cells, there are still some research gaps. First, implementing wavelet transform in the embedded system is still not easy since many times of addition and multiplication are required compared with the Fourier transform. On the other hand, although SFT improves the performance of nonstationary signals, the fixed window width still cannot efficiently analyze the interference signals with rich harmonics. Accordingly, how to realize online impedance calculation with less computing resources while taking into account both accuracy and robustness remains a challenge. Second, it is known that the operating conditions of the fuel cell are complex in vehicular applications. However, the broadband impedance spectrum online acquisition technology mentioned earlier is insufficiently harnessed under different operating conditions, especially fault states, such as membrane drying, flooding, and starvation. Inaccurate online impedance measurement may result in these failures not being detected in time, leading to irreversible attenuation like platinum and carbon dissolution.

To bridge the research gap, as the main contributions of this article, an advanced online broadband impedance spectrum acquisition scheme of PEM fuel cells is proposed. First, rather than wide bandwidth signals usually used in previous articles, an excitation device composed of a signal generator and a power amplifier is designed to generate the square wave signal. Second, a transformation method based on Fourier transform with adaptive Gaussian window, namely, S-transform (ST), is selected for calculating the broadband impedance spectrum of PEM fuel cells. Such adaptive ability of window width to frequency makes ST stronger than SFT in processing nonstationary signals, and at the same time, preserving high computational efficiency. Third, the effectiveness and resilience of the ST are deeply validated under different excitation currents conditions (considering excitation amplitude, slope, and period), current densities, cell temperatures, and even fault scenarios (drying, starvation, and flooding) of different levels, as well as different stable time before measurement. Moreover, the performance of ST and the popular method based on MWT in method of the latest papers are compared from calculated accuracy and consumed time.

II. METHODOLOGY

A. Fundamentals of ST

First, for the time domain signal $x(t) \in L^2(R)$, its SFT can be given as [25]

$$F(f, \tau) = \int_{-\infty}^{\infty} x(t)h(t - \tau)e^{-j2\pi ft}dt \quad (1)$$

where $h(t - \tau)$ stands for the rectangular window; τ is the moment of frequency analysis; f is the frequency of the harmonics

analyzed. Rather than taking an infinitely long trigonometric function $e^{-j2\pi ft}$ as the basis function, the finitely long decaying wavelet basis is applied in MWT and can be expressed as [16]

$$W_{a,b} = \int_{-\infty}^{\infty} x(t)\psi(t_m) dt \quad (2)$$

where $\psi(t_m)$ is the Morlet wavelet basis, and represented as

$$\psi(t_m) = \frac{1}{\sqrt{\pi f_b}} e^{j2\pi f_c t_m} e^{-t_m^2/f_b} \quad (3)$$

in which f_b represents the band parameter; f_c is the center frequency; $t_m = (t - b)/a$ is the time of the mother wavelet; a is the scale parameter, controlling the shape of $\psi(t_m)$; b is the time parameter, determining the center position of $\psi(t_m)$. By flexibly changing a and b , WFT shows greater flexibility in time and frequency resolution than the SFT.

For the time domain signal $x(t) \in L^2(R)$, its S-T is defined as follows [31]:

$$S(\tau, f) = \int_{-\infty}^{\infty} x(t)g(t - \tau)e^{-j2\pi ft} dt \quad (4)$$

where $g(t - \tau)$ is the Gaussian function, and expressed as

$$g(t - \tau) = \frac{|f|}{\sqrt{2\pi}} e^{-\frac{(\tau-t)^2 f^2}{2}}. \quad (5)$$

Let the basis function of ST be $s(t)$, its time–frequency window characteristics reflect the resolution of ST in the time–frequency domain. Define $s(t)$ at $f = 1$ and $\tau = 0$ as the standard state $s_{\text{std}}(t)$, which is shown as

$$s_{\text{std}}(t) = \frac{1}{\sqrt{2\pi}} e^{-\frac{1}{2}} e^{j2\pi t}. \quad (6)$$

The center and radius of the time window of $s(t)$ in general form are denoted as t_s and Δt_s , respectively. The relationship between the center and radius of the time window in the general state and the standard state $(t_{s,\text{std}}, \Delta t_{s,\text{std}})$ can be deduced as

$$t_s = \frac{t_{s,\text{std}}}{f} + \tau, \Delta t_s = \frac{\Delta t_{s,\text{std}}}{f}. \quad (7)$$

Similarly, define that the general frequency window center and radius of $s(t)$ are ω_s and $\Delta\omega_s$, respectively, and deriving

$$\omega_s = f\omega_{s,\text{std}}, \Delta\omega_s = f\Delta\omega_{s,\text{std}} \quad (8)$$

where $\omega_{s,\text{std}}$ and $\Delta\omega_{s,\text{std}}$ are center and radius of the frequency window in the standard state, respectively. Two salient observations can be made from (7) and (8). First, τ only affects the position of the basis function $s(t)$ in the time domain so that various local signals can be analyzed by varying τ . Second, $s(t)$ can be updated adaptively according to the change of frequency. The waveform of $s(t)$ in the time–frequency domain at different frequencies ($\tau = 0$) is shown in Fig. 1. It is observed that the time window width of ST gradually decreases as f increases, and the width and center frequency of the frequency window increase progressively. This narrower time window provides better time resolution so that ST can better extract the high-frequency components in the signal. On the contrary, the narrower frequency window provides better frequency resolution, while the wider time window ensures the acquisition of

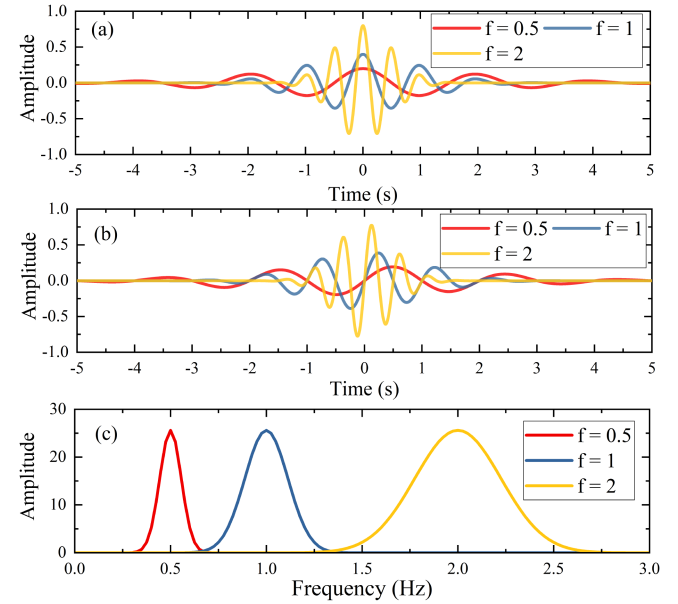


Fig. 1. $S(t)$ at different frequencies; (a) real part of time-domain waveform; (b) imaginary part of time-domain waveform; and (c) frequency-domain waveform.

LF component information. Moreover, the frequency domain waveform of ST is generally narrow and sharp, and both sides of the central frequency will rapidly decay to zero, hence these features effectively reduce the main lobe width and side lobe height to suppress the influence of harmonics and improve the signal leakage in time–frequency analysis.

In general, ST is a time–frequency analysis method between Fourier transform and wavelet transform, which is the inheritance and development of both. On one side, it has a time-scale analysis ability similar to wavelet transform, and meanwhile FFT can be used to improve its computational efficiency. On the other side, it also alleviates the problem that the window width of SFT cannot be adjusted with frequency, thus providing unique conditions for its application in fuel cell impedance calculation.

B. Impedance Calculation Based on S-T

By applying ST to the excitation current $I(t)$ and response voltage $U(t)$, the impedance Z of the PEM fuel cell is calculated as

$$Z(\tau, f) = \frac{S_U(\tau, f)}{S_I(\tau, f)} = \frac{\int_{-\infty}^{\infty} U(t) \frac{|f|}{\sqrt{2\pi}} e^{-\frac{(\tau-t)^2 f^2}{2}} e^{-j2\pi ft} dt}{\int_{-\infty}^{\infty} I(t) \frac{|f|}{\sqrt{2\pi}} e^{-\frac{(\tau-t)^2 f^2}{2}} e^{-j2\pi ft} dt} \quad (9)$$

where $S_U(\tau, f)$ and $S_I(\tau, f)$ represent ST for voltage and current, respectively. To increase computational efficiency, we can make

$$\begin{cases} U'(t) = U(t) \frac{|f|}{\sqrt{2\pi}} e^{-\frac{(\tau-t)^2 f^2}{2}} \\ I'(t) = I(t) \frac{|f|}{\sqrt{2\pi}} e^{-\frac{(\tau-t)^2 f^2}{2}}. \end{cases} \quad (10)$$

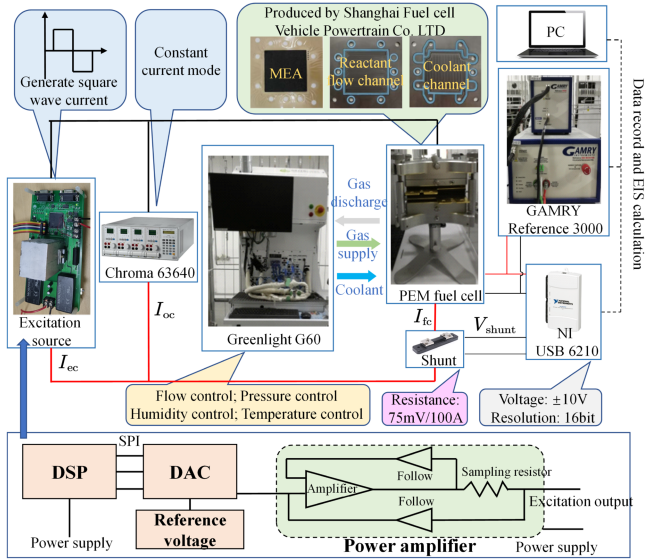


Fig. 2. Schematic diagram of the fuel cell impedance test system.

Based on (10), then (9) can be rewritten as

$$Z(\tau, f) = \frac{\int_{-\infty}^{\infty} U'(t) e^{-j2\pi ft} dt}{\int_{-\infty}^{\infty} I'(t) e^{-j2\pi ft} dt} = \frac{F_{U'}(\tau, f)}{F_{I'}(\tau, f)} \quad (11)$$

where $F_{U'}(\tau, f)$ and $F_{I'}(\tau, f)$ are the Fourier coefficients of $U'(t)$ and $I'(t)$, respectively. Then, FFT can be applied for accelerating convolution operation. Moreover, note that the Gaussian function conforms to the normal distribution principle, its integral area can reach 99.72 % of the total integral area when time t is between $\tau - 3\sigma$ and $\tau + 3\sigma$. In contrast, the Gaussian function will approach 0 indefinitely as t is less than $\tau - 4\sigma$ or greater than $\tau + 4\sigma$. Hence, the interval of integral operation can be adjusted from $(-\infty, \infty)$ to $(\tau - 4\sigma, \tau + 4\sigma)$, and (11) can be changed as

$$Z(\tau, f) = \frac{\int_{\tau-4\sigma}^{\tau+4\sigma} U'(t) e^{-j2\pi ft} dt}{\int_{\tau-4\sigma}^{\tau+4\sigma} I'(t) e^{-j2\pi ft} dt}. \quad (12)$$

III. EXPERIMENTAL AND IMPLEMENTATION

A. Experimental Setup

The test bench and related connection is displayed in Fig. 2. A single PEM fuel cell with the active area of 50 cm^2 produced by Shanghai Fuel cell Vehicle Powertrain Co. LTD is tested here, where the flow field within anode/cathode bipolar plate is three-channel snake flow field, and the coolant flow channel is parallel straight structure. The test bench provides the fuel cell with the target mass flow, humidity and pressure of the reactant, while keeping the cell temperature constant through a coolant loop. The operating current I_{oc} is controlled by a commercial electronic load. To generate the excitation current I_{ec} , an additional excitation source is designed and connected in parallel to the load bus. Besides, a shunt resistance $R_{shunt} = 0.75 \text{ m}\Omega$ is connected in series near the fuel cell, and its voltage drop V_{shunt}

TABLE I
FUEL CELL SWC

Name	Symbol	Unit	Value
Current density	I_{oc}	A/cm^2	1.0
Stoichiometry (cathode/anode)	$\lambda_{ca}/\lambda_{an}$	-	2.5/1.5
Inlet pressure (cathode/anode)	p_{ca}/p_{an}	kPa	150/160
Relative humidity (cathode/anode)	RH_{ca}/RH_{an}	%	50/60
Cell temperature	T_{cell}	$^\circ\text{C}$	75

can be measured by a data acquisition card and used for fuel cell current I_{fc} calculation ($I_{fc} = V_{shunt}/R_{shunt}$). It is remarked that the calculation of impedance depends on the sampling accuracy of the current, so the working current should be within the specified range of the shunt to prevent temperature drift from having a significant impact on the calculation accuracy. The fuel cell terminal voltage V_{fc} is also collected. The electrochemical workstation measures the reference EIS of the PEM fuel cell to verify the accuracy of ST algorithm. A laptop computer with a processor of 1.6 GHz and 8 GB RAM is applied to record the data and run the calculation program developed by MATLAB R2015b.

B. Excitation Device Design

The excitation device is composed of a signal generator and a power amplifier, and its basic circuit principle is also shown in Fig. 2, where the signal generator contains a digital signal processor (DSP) and digital-to-analog converter (DAC). The DSP of Texas Instruments (TI) TMS320F2812 is used here, which is a 32-b micro control unit with a clock speed of up to 150 MHz and capable of controlling the period and amplitude of square wave excitation in impedance measurement through the built-in timer period adjustment and register shift. The DAC in the signal generator adopts TI DAC8831, and the reference voltage generated by Analog Devices ADR421 is selected as 2.5 V.

The output current of the DAC in the waveform generator is usually several millamps to tens of millamps, while the excitation current required for fuel impedance measurement is generally greater than 1 A. Therefore, the excitation waveform output from the DAC demands to be amplified by a power amplifier. Here, the core of the power amplifier is designed by TI OPA549, which can carry up to 10 A peak output current. At the same time, to output stable square wave current, differential voltage feedback followed by TI OPA227 is introduced. Ultimately, the excitation current of the target amplitude can be conveniently obtained through appropriate sampling resistance configuration by means of making the sampling resistor voltage equal to the excitation voltage of the DAC output.

C. Experimental Procedures

First, the standard working condition (SWC) based on frequently used stoichiometry, pressure, humidity, and temperature in actual vehicular fuel cell system, is established prior to reference EIS testing and listed in Table I. All reference EIS

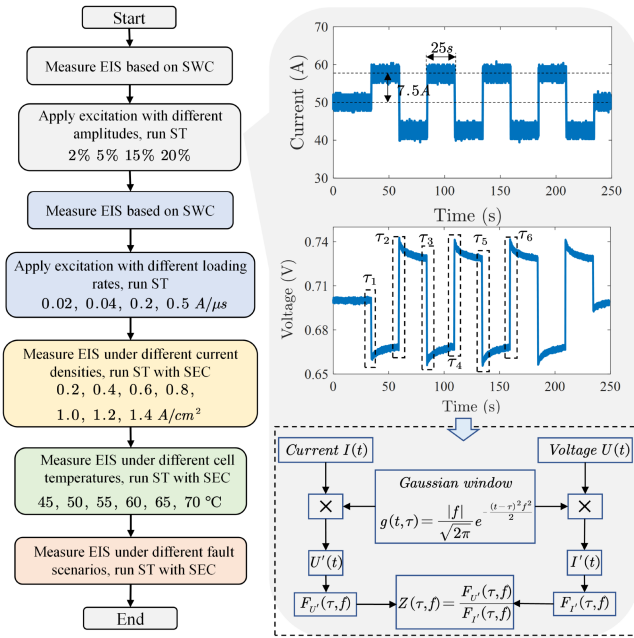


Fig. 3. Testing procedures of the impedance calculation based on ST.

experiments were carried out under the galvanostatic mode by sweeping frequencies covering 1 kHz to 0.1 Hz with 12 points per decade (more points selected per decade, the smoother the measured impedance spectrum, especially under fault scenarios), because for one, a small voltage disturbance can cause a considerable change in current, for another, such the frequency band is convinced to be capable of covering most of the polarization processes within the PEM fuel cell. In particular, the alternating current amplitude generated by the workstation was picked up to be 8% of direct current to achieve a linear measure, and there was about 15–20 min for sufficient stabilization before every reference impedance measurement. Based on this, a standard excitation current (SEC) of periodic square wave is defined. In details, the excitation amplitude is also selected as 8% of operating current. Moreover, the loading rate or unloading rate at each jumping moment of the SEC is $0.05 \text{ A}/\mu\text{s}$ to locate enough data point on the transient edge. Meanwhile, considering that the period of the excitation signal should be at least twice that of the lowest analysis frequency of 0.1 Hz, the period of the SEC is selected 50 s to guarantee the calculated accuracy at the LF band.

To investigate the validity of proposed impedance acquisition method for the PEM fuel cell, different excitation current forms, and external operating conditions are considered. The whole process is presented in Fig. 3. First, the reference EIS was measured under the SWC. Then, periodic square wave excitation currents with various excitation amplitudes were applied in turn through the designed excitation device. The data acquisition card recorded the voltage of both fuel cell and shunt with 10 kHz sampling frequency, and this sampling frequency is considered high enough to alleviate signal aliasing to ensure impedance calculated accuracy. Besides, the duration of each excitation

TABLE II
FUEL CELL FAULT OPERATING CONDITIONS

Fault level	I_{oc} A/cm ²	T_{cell} °C	$\lambda_{ca}/\lambda_{an}$	RH_{ca}/RH_{an} %/%	p_{ca}/p_{an} kPa/kPa
Starvation conditions					
Minor	1.0	75	1.7/1.5	50/60	150/160
Moderate	1.0	75	1.5/1.5	50/60	150/160
Severe	1.0	75	1.3/1.5	50/60	150/160
Flooding conditions					
Minor	1.5	65	2.2/1.5	70/80	150/160
Moderate	1.7	60	2.0/1.5	80/90	150/160
Severe	1.7	55	1.7/1.5	90/100	150/160
Drying conditions					
Minor	0.5	75	2.5/1.5	20/50	150/160
Moderate	0.4	80	2.7/1.5	10/50	150/160
Severe	0.3	85	3.0/1.5	0/50	150/160

current was not less than three cycles. An example of 15% amplitude excitation is given in the figure, where blue-filled bands are the measurement noise. Six moments τ_1 to τ_6 were selected at the jumping moments of the excitation current signal by an automatic search process proposed in [16] since high-frequency harmonics are mainly concentrated at the step time. By this, six impedance spectrums at the specific moment can be calculated based on (12) by convolving the original current and voltage with the Gaussian window. The final impedance spectrum can be obtained by taking the average of six calculated impedance to reduce error.

Similarly, the effects of the slew rate and period of excitation current, as well as impedance calculation under other operating conditions can be analyzed on the basis of the above steps. The current density changed from 0.2 to $1.4 \text{ A}/\text{cm}^2$ to cover the activation loss, ohmic loss, and concentration loss range of the PEM fuel cell, and the temperature was adjusted from 45 to 70°C to cover the operating temperature range of the fuel cell system as much as possible. In decoupling analysis of these impacts on ST calculation, the control variable method is introduced, that is, all working conditions and excitation conditions remain as standard values, except for the parameter or condition being analyzed. Moreover, typical vehicular fuel cell faults, such as air starvation, cathode flooding, and membrane drying were also performed to test the ST ability for impedance calculation. The detailed fault conditions are listed in Table II and established based on fault causes in [32], where cathode stoichiometry was sequentially reduced to reproduce the air starvation from the perspective of directly reducing the oxygen supply. On the other hand, to create a flooding fault, the operating temperature was lowered to promote vapor condensation. At the same time, higher inlet humidity, higher current density, and lower air stoichiometry were also recommended in the flooding experiment in view of weakening convection in the flow channel and more water produced at the cathode side. Membrane drying is usually the opposite of flooding fault, and its occurrence can adjust operating conditions in the reverse direction of flooding experiments.

TABLE III
ACCURACY AND EFFICIENCY OF MWT AND ST AGAINST DIFFERENT EXCITATION CURRENT

Excitation set	MWT			ST		
	RMSE mΩ · cm ²	Mean RE %	Time s	RMSE mΩ · cm ²	Mean RE %	Time s
2%	8.83	5.51	32.12	9.29	5.83	1.78
5%	3.69	2.44	32.43	4.86	2.96	1.81
15%	4.38	2.35	32.34	4.27	2.31	1.68
20%	4.70	2.99	32.12	3.48	1.97	1.70
0.02A/μs	12.67	6.83	32.13	10.80	4.95	1.69
0.04A/μs	4.61	3.87	30.89	3.81	2.24	1.70
0.2A/μs	6.65	3.72	31.87	2.87	1.83	1.68
0.5A/μs	7.99	5.12	32.01	3.15	1.49	1.71
2 s	7.15	3.34	31.39	5.96	3.25	1.96
15 s	6.64	3.48	31.52	4.87	3.04	1.87
30 s	6.36	3.22	32.14	4.71	2.80	1.91
50 s	3.51	2.64	31.98	3.76	2.73	1.87

IV. RESULTS AND DISCUSSION

A. Impedance Calculation Under Different Excitation Conditions

To examine the robustness of the proposed calculation scheme against different excitation forms, square wave signals with various amplitudes, slopes, and periods were generated through the designed excitation device. Moreover, MWT was also applied in impedance calculation to highlight the computational efficiency of ST. As for critical parameters of MWT, the center frequency f_c is selected as 10 kHz as large as possible to improve the time resolution of the signal and eliminate the small noise of the signal. Besides, the center frequency of the subwavelet should be the same as the frequency of the measured EIS f , and hence scale parameters a were selected from 10^5 to 10 based on $a = f_c/f$, corresponding to 49 frequency points of the EIS between 0.1 Hz and 1 kHz. The analysis moment b can be selected as the jump moment of the excitation signal to obtain a more accurate high-frequency impedance since the high-frequency component of the square wave signal is mainly concentrated at the step moment, which is the same as the analysis moment τ of ST. Moreover, the band parameter f_b is determined by $T^2/(32a_{\max}^2) = 7.8 \times 10^{-9} s^2$ based on the standard that the integration interval of the Gaussian window of the subwavelet with the lowest center frequency is equal to the period of the excitation current T , and more details can be located in [16].

By implementing the ST and MWT, the obtained results and reference impedance premeasured are given in Fig. 4 and Table III. To characterize the calculated performance, other than consumed time, the root mean square error (RMSE) and relative error (RE) with the definition of

$$\text{RMSE} = \sqrt{\frac{1}{N} \sum_{i=1}^N (Z_{\text{mea},i} - Z_{\text{cal},i})^2} \quad (13)$$

$$\text{RE}(i) = \left| \frac{Z_{\text{cal},i} - Z_{\text{mea},i}}{Z_{\text{mea},i}} \right| \times 100\% \quad (14)$$

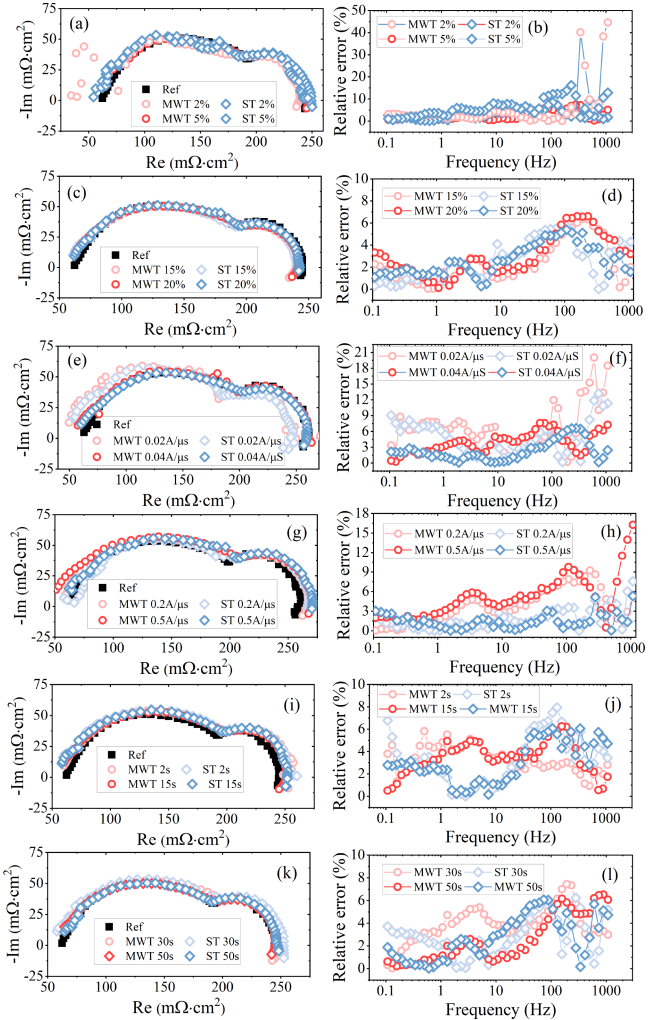


Fig. 4. Validation of the ST and MWT against measured EIS under different excitation conditions (a–d, excitation amplitude; e–h, step slope; i–l, signal period).

are used, where $N = 49$ stands for 49 frequency points in the impedance spectrum; Z_{mea} is the measured impedance; $Z_{\text{cal},i}$ represents the calculated impedance by ST or MWT. Based on this, observations and remarks can be made as follows:

- Both ST and MWT can effectively obtain impedance spectrum based on different excitation signals, and two obvious capacitive loops can be observed, as the same as tested results. In terms of excitation amplitude, it is widely accepted that the amplitude range of 5%–10% is suitable for a tradeoff between signal-to-noise ratio (SNR) and linear measurement [9]. Hence, as expected, the excitation amplitude of 2% shows relative poor performance and the amplitude of 5% can significantly improve calculated accuracy, also, further strengthening excitation amplitude can obtain higher precision.
- The calculated impedance spectrum with 0.02 A/μs has a significant error because of not concentrating frequency information with a slower step slope. As further increasing step slope, the impedance spectrum calculated by ST

and MWT is basically consistent with that measured by the electrochemical workstation. However, the RMSE of $0.5 \text{ A}/\mu\text{s}$ is larger than that of $0.2 \text{ A}/\mu\text{s}$, because the overshoot of the excitation current (not plotted here) may occur at the step time with a significant slope requirement due to the control precision of the excitation device.

- 3) Under the excitation with period 2 s, the RE of LF (e.g., from 0.1 to 10 Hz) impedance is significant, and the reconstructed impedance spectrum is not smooth. With the increase of the excitation period, the RE of the LF impedance decreases. Especially, the RE calculated by ST is less than 4% at LF as long as the excitation period is greater than 15 s, showing satisfactory accuracy.
- 4) The ST can, in general, more accurately realize the EIS acquisition, as compared to the MWT. What is more striking is that the calculation time of ST is much smaller than that of MWT. These algorithms were executed in M-files of MATLAB and time was recorded using *tic* and *toc*. It can be found that the calculated time with ST can be saved by nearly 94.3% (MWT: 32 s, ST: 1.7 s). Meanwhile, the excitation period of 15 s can obtain enough accuracy, and hence it only takes 45 s for continuous excitation to realize six times of impedance spectrum calculation, which reduces huge time taken for traditional sweeping method of workstation (signal duration is around 14 min for the frequency range 0.1 Hz to 1 kHz with six times measurement at each frequency point). These dispenses an enormous advantage of broadband impedance measurement based on ST and square wave excitation in terms of computational speed and is more conducive to online vehicular applications.
- 5) Perfect calculation with tiny errors, e.g., 1% RE, is extremely hard for all frequency. This, on the one hand, is because of limited measurement accuracy of acquisition card itself, and on the other hand, the amplitude of harmonics in a step signal is minimal at the high-frequency range, leading to a limited SNR for the high-frequency impedance calculation.

B. Impedance Calculation Under Different Current Densities and Cell Temperatures

1) *Current density*: To validate the ST along the polarization curve, the series of reference EIS, operating current, and response voltage measurements were made from $0.2 \text{ A}/\text{cm}^2$ to as high as $1.4 \text{ A}/\text{cm}^2$. During the test process, the reactant stoichiometry, inlet pressure, relative humidity, and cell temperature were set as in Table I. The measured EIS and calculated impedance spectrum are presented in Fig. 5. Also, the specific comparison results are listed in Table IV. As can be seen, the middle-frequency arc determined by the charge transfer kinetics decreases first as the current density increases to $1.0 \text{ A}/\text{cm}^2$ because of the increment in driving force for the oxygen reduction reaction. But it increases slightly as further increases the current density since a large amount of generated water accumulates in the porous media, hindering the oxygen transfer and eventually decreasing the oxygen concentration on the reaction site, causing

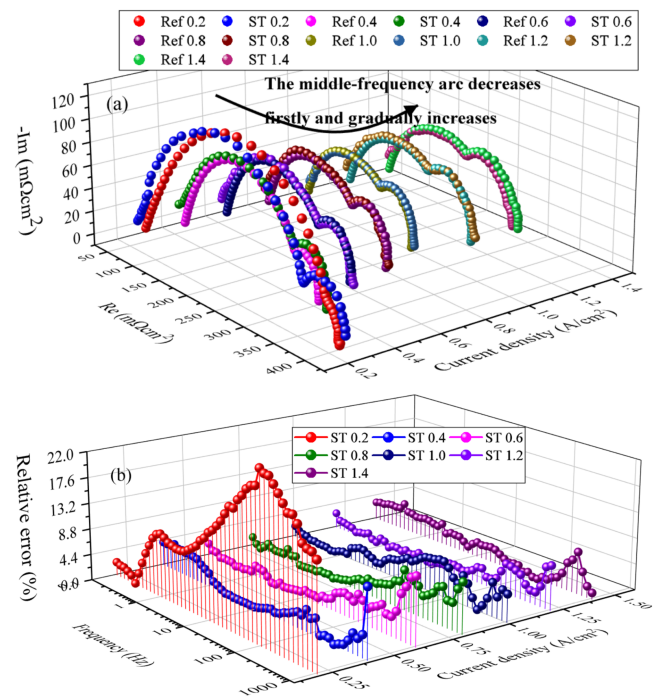


Fig. 5. Calculated impedance spectrum (a) by ST and (b) RE under different current densities.

TABLE IV
ACCURACY AND EFFICIENCY OF MWT AND ST AGAINST DIFFERENT CURRENT DENSITIES

Current A/cm ²	MWT			ST		
	RMSE mΩ · cm ²	Mean RE %	Time s	RMSE mΩ · cm ²	Mean RE %	Time s
0.2	29.89	11.18	33.43	37.79	14.59	2.09
0.4	5.61	2.28	31.07	6.43	2.09	2.02
0.6	3.69	2.17	35.39	3.63	2.39	1.98
0.8	3.87	2.67	35.70	3.79	2.52	2.05
1.0	3.42	2.53	34.36	4.45	2.70	2.09
1.2	4.56	2.43	33.73	2.77	1.79	1.93
1.4	6.9	4.09	34.8	6.18	2.52	2.16

a considerable concentration loss, and also therefore LF loop size increases. The intercept at high frequency indicating ohmic loss decreases with the increase of current density attributed to a better hydration state. The calculated impedance spectrum by ST and MWT can both follow the measurement trajectories by the workstation with acceptable accuracy, and especially the ST presents remarkable computational efficiency compared to MWT. However, in terms of the current density of $0.2 \text{ A}/\text{cm}^2$, a considerable RE outstripping 10% can be observed, potentially attributed to the poor SNR for small operating current and exciting current.

2) *Cell Temperature*: The coolant temperature of the fuel cell system changes with the working current. By this, the EIS measurement and impedance spectrum calculation were carried out from 45 to 70 °C (other operating conditions are the same as Table I). Calculated results by ST are shown in Fig. 6, and detailed comparisons are listed in Table V. It can be seen that the

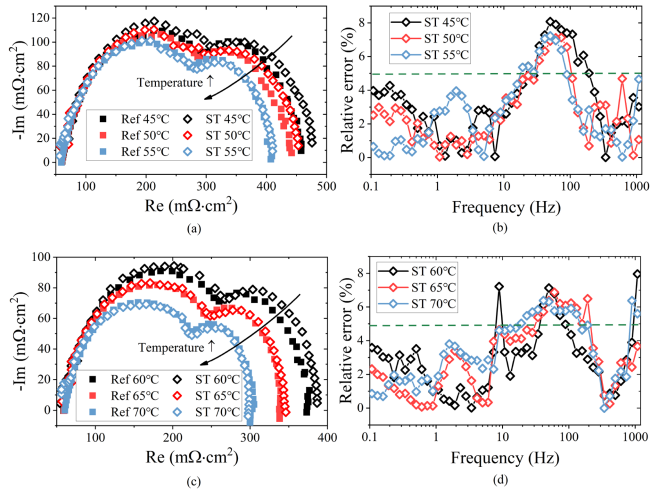


Fig. 6. Calculated impedance spectrum by ST and its RE under different cell temperature.

TABLE V
ACCURACY AND EFFICIENCY OF MWT AND ST AGAINST DIFFERENT TEMPERATURES

Temperature °C	MWT			ST		
	RMSE $\text{m}\Omega \cdot \text{cm}^2$	Mean RE %	Time s	RMSE $\text{m}\Omega \cdot \text{cm}^2$	Mean RE %	Time s
45	24.29	8.21	32.72	9.28	3.42	2.15
50	19.06	6.65	33.07	6.89	2.70	2.03
55	7.97	4.61	34.54	6.81	2.66	2.32
60	12.22	6.08	33.72	7.05	2.85	2.37
65	6.76	4.07	33.98	6.07	2.95	2.12
70	4.83	3.17	34.17	6.50	3.34	2.13

middle-frequency arc decreases as increasing temperature since improving temperature can increase the possibility of reactants reaching the activated state. Besides, the LF arc also decreases due to more effortless mass transfer (higher temperature corresponds to greater saturated vapor pressure and oxygen diffusion coefficient). The ohmic loss only changes slightly because the membrane can be fully humidified with adequate intake humidity and generated water at operating current density 1.0 A/cm^2 . As expected, ST can also satisfactorily describe the trend of measured EIS with temperature, as evidenced by the RE of less than 5% for most frequency bands and the mean RE of less than 4%. Meanwhile, the computation time was saved by nearly 94% compared with MWT, and the accuracy was generally relatively higher.

C. Impedance Calculation Under Different Fault Scenarios

The fuel cell will inevitably suffer faults if external operating conditions are not adequately controlled. To further study the ST performance for EIS calculation under different fault scenarios, the air starvation, flooding, and drying experiments based on **Table II** were conducted. The obtained results by the ST are shown in **Fig. 7** and detailed indicators are given in **Table VI**,

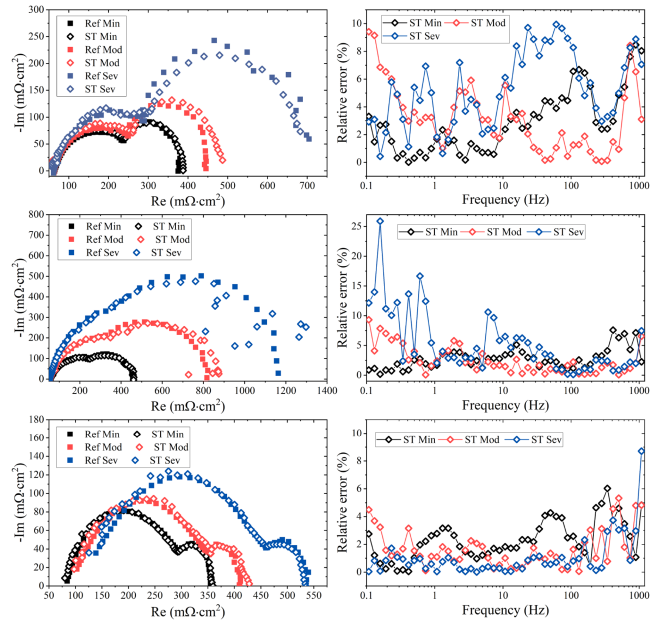


Fig. 7. Calculated impedance spectrum by ST and its RE under different degrees of starvation fault (first line), flooding fault (second line), and drying fault (third line).

TABLE VI
ACCURACY AND EFFICIENCY OF MWT AND ST UNDER VARIOUS FAULTS

Fault degree	MWT			ST		
	RMSE $\text{m}\Omega \cdot \text{cm}^2$	Mean RE %	Time s	RMSE $\text{m}\Omega \cdot \text{cm}^2$	Mean RE %	Time s
Starvation Min	7.53	2.86	32.58	5.19	2.89	2.06
Starvation Mod	20.24	7.08	33.82	13.54	3.18	2.03
Starvation Sev	23.15	5.83	32.51	15.67	5.25	2.17
Flooding Min	6.6	4.47	32.77	6.53	2.73	2.21
Flooding Mod	23.47	7.51	33.05	21.4	2.94	2.14
Flooding Sev	92.1	8.34	31.87	74.7	5.33	2.09
Drying Min	3.74	1.65	32.11	5.56	2.31	2.23
Drying Mod	9.3	3.32	33.41	5.92	1.69	2.16
Drying Sev	9.61	2.79	32.64	6.09	1.36	2.08

where “Min,” “Mod,” and “Sev” in the legend represent the three fault levels of minor, moderate, and severe, respectively.

It can be observed that, despite facing air starvation, the calculation by ST for impedance spectrum can still well follow its actual values with acceptable accuracy of 10% and demonstrate relatively better results compared to MWT. In addition, it can be seen that the imaginary part of the lowest frequency impedance is farther away from the real axis with more severe air starvation, indicating the greater oscillation amplitude of the oxygen concentration in the catalyst layer [13]. Similar calculation performance can be achieved under the flooding scenario. However, it is clear that there is a large error (mean RE outstrips 10%, RMSE is as high as $74.7 \text{ m}\Omega \cdot \text{cm}^2$) in the LF range against severe flooding fault, because the PEM fuel cell is easy to enter the nonlinear or unstable state alongside of the normal working conditions. As a result, the output voltage fluctuation is significant, which brings great challenges to the EIS measurement and calculation. Fortunately, on the basis of ST technology, it is also able to diagnose impedance spectrum for moderate flooding

TABLE VII
COMPARISON OF MAINSTREAM ON-LINE FUEL CELL IMPEDANCE CALCULATION METHODS

Ref	Excitation	Frequency range	Verification	Processing method	Remarks
[21]	sinusoidal signal	320 Hz	N/A	fast Fourier transform	- long time by sweeping frequency
[25]	Chirp signal	0.1 Hz - 10 kHz	predefined ECM (error not given)	short-time Fourier transform	- cannot adapt to frequency change
[26]	multiple sinusoidal signal	0.1 Hz - 10 kHz	single EIS (error not given)	fast Fourier transform	- lack of time domain information - excitation device design is complex
[29]	pseudo-random binary sequence	0.1 Hz - 500 Hz	single EIS (error not given)	Morlet wavelet transform	- faster acquisition compared to sweeping method
[24]	pseudo-random binary sequence	0.5 Hz - 500 Hz	single EIS (error not given)	Morlet wavelet transform	- excitation device design is complex
[30]	square wave signal	0.1 Hz - 1 kHz	predefined ECM (error not given)	Morlet wavelet transform	- convolution at each moment of the original signal
[16]	square wave signal	0.1 Hz - 1 kHz	EIS under various excitation (error not given)	Morlet wavelet transform	- faster acquisition compared to sweeping method
Here	square wave signal	0.1 Hz - 1 kHz	EIS under different excitation, current, temperatures, and faults (RMSE and mean RE)	S-transform	- excitation device design is simple - convolution only at several jump moments - calculated time saved nearly 95% compared with MWT - better robustness compared with MWT

failures in a timely manner so that we can adjust operating conditions in advance with impedance-based feedback control to avoid severe flooding. When membrane drying fault is more serious, it is evident that high-frequency impedance gradually increases, and middle-frequency arc increases because of current reduction and cut-off of the proton transport path inside cathode ionomer. But generally speaking, the membrane drying mainly occurs in the low current range, and it will be alleviated under high current density by self-humidification [33]. Or, open the bypass of the air inlet to prevent excess air from entering the stack to purge moisture at low current density. Therefore, high-frequency impedance in fuel cell system controller is mainly for shutdown purging control to improve the success rate of cold start. The RE of high-frequency impedance from 300 Hz to 1 kHz calculated by ST is basically within 6%, presenting a satisfactory accuracy, and the calculation efficiency is much higher than MWT.

D. Impedance Calculation Under Different Stable Time

The impedance spectrum is usually measured in a steady state. Achieving on-board impedance measurement is to force the fuel cell vehicle to be stable for a while, and hence impedance measurement at different stable time was tested. In detail, first, measure the reference impedance spectrum under the SWC and stabilize for 10 min. Make the fuel cell oscillate between 0.6 A/cm^2 and 1 A/cm^2 with a period of 60 s and repeat the oscillation five times. Then, wait for different stable time and apply the standard excitation current to the fuel cell, recording the current and voltage simultaneously.

Fig. 8 shows the results for the stable time ranging from 10 s to 20 min. It can be seen that the calculated impedance gradually approaches the reference value as increasing stable time. Both RMSE and mean RE by ST and MWT decrease rapidly in the first 30 s, where the ST presents better performance, supported by that mean RE is less than 3% based on the stable time 10 s. With these in mind, it is more convenient to calculate the broadband impedance spectrum in the dynamic condition of the fuel cell vehicle by using ST because of less required stable time.

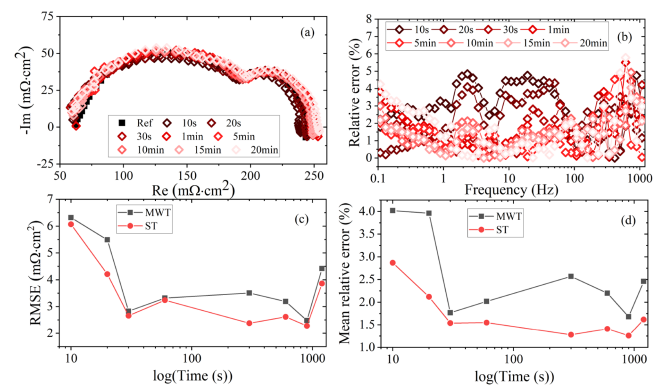


Fig. 8. Calculated impedance spectrum (a), RE (b), RMSE (c) and mean RE (d) under different stable time.

E. Concise Argumentation

The acquisition methods of the online impedance spectrum of the PEM fuel cell are summarized in Table VII. The method proposed here has the characteristics of fast acquisition speed and easy hardware implementation, which is very suitable for online management of fuel cell system. At present, experiments are carried out on a single fuel cell. It is necessary to apply this method to stack scale and even fuel cell system, and some considerations are remarkable. First, the shunt is used here to convert its voltage into the operating current of the fuel cell. The high-power stack with a large operating current has requirements on the temperature drift and working current range of the shunt. In the future, when designing the actual measurement system, other current measurement schemes, such as high-precision and high-response rate current sensors, can be selected comprehensively considering the cost and reliability. The other is that the excitation device based on power amplifiers may not satisfy large excitation requirements, and hence design of the square wave excitation source needs to meet the high current and voltage requirement, as well as heat dissipation capacity. For example, the dc/dc-based excitation source can be regarded as one of the suitable choices for the system application. Besides, multichannel synchronous voltage sampling can also be designed for measuring impedance of each cell in the stack,

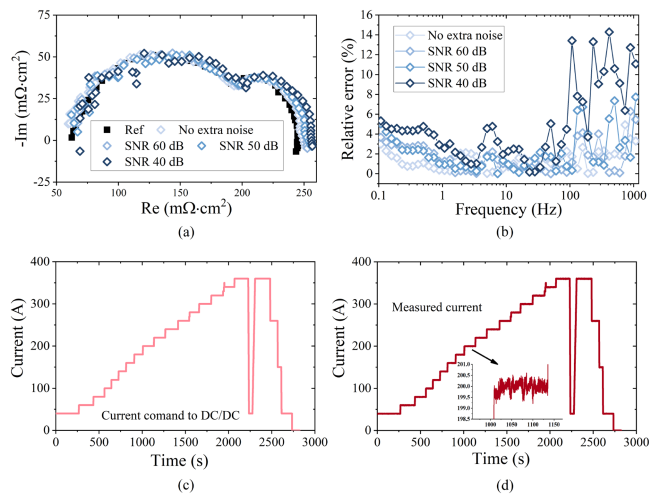


Fig. 9. Calculated impedance spectrum and RE with extra noise (a, b); current command and measured current of a 90-kW fuel cell system (c, d).

which can be used for advanced cell consistency management to further improve the stack life except for voltage information.

In an actual fuel cell system, some high-voltage components, such as air compressor, hydrogen cycle pump, water pump, and dc/dc, may impact the current and voltage acquisition because of electromagnetic compatibility effects. Also, for commercialized dc/dc with current control mode, there exists the triangular ripple with frequency 320–400 kHz and amplitude 1%–2% of dc. Current ripple can also be collected as noise by the data acquisition card. Therefore, the current and voltage data measured under the SWC are added with different SNR Gaussian noises to simulate the influence of these components on the ST algorithm. Besides, a section of current data of a 90 kW fuel cell system is captured to determine the measurement noise at the system scale, in which the current instruction sent to dc/dc is regarded as the original data, and the measured current is considered as the data containing noise. Based on this, the calculated SNR for the current measurement of the fuel cell system is about 48.3 dB. As shown in Fig. 9, the REs of all frequencies are less than 8% by adding 60 and 50 dB of extra noise to the original measured data, indicating that the ST algorithm can almost present acceptable results under the environment of the fuel cell system. The RE of the frequency higher than 100 Hz is basically greater than 10% when the added noise is 40 dB, while the RE of the impedance frequency lower than 100 Hz is less than 6%, which can still be used for LF loss assessment to avoid gas shortage or water flooding failure.

V. CONCLUSION

This article devises an online broadband impedance spectrum acquisition scheme of PEM fuel cells based on S-T, in which the Gaussian window width can adapt to the frequency to be qualified for nonstationary signal processing, and meanwhile, the computational efficiency can be improved by FFT. Besides, an excitation source composed of a signal generator and a power

amplifier was designed to generate the square wave excitation current, which can realize different excitation amplitude, variable load slope, and period settings. Based on this, the performance of ST and MWT are compared under different operating conditions. The experimental results indicated that the excitation current amplitude should not be too small, and too fast or slow step rate is not conducive to impedance calculation. Furthermore, the robustness of the proposed ST-based scheme against the current density, cell temperature, fault scenarios (starvation, flooding, and drying), stable time, and system-level noise environment has also been verified. Experimental results showed that the ST can yield a sustained performance in impedance calculation against a wide range of operating conditions, except for the current of 0.2 A/cm² and severe flooding fault. Fortunately, the severe flooding fault can be avoided in advance since the ST can reproduce impedance measured under medium flooding fault accurately. In addition, the ST has demonstrated higher computation efficiency than that of MWT, as approved by that calculation time can be saved by nearly 95%. The ST also shows better robustness compared with the MWT, which is more suitable for online vehicular applications.

REFERENCES

- [1] Z. Hua, Z. Zheng, E. Pahon, M.-C. Péra, and F. Gao, “A review on lifetime prediction of proton exchange membrane fuel cells system,” *J. Power Sources*, vol. 529, 2022, Art. no. 231256.
- [2] H. Yuan, H. Dai, X. Wei, and P. Ming, “Model-based observers for internal states estimation and control of proton exchange membrane fuel cell system: A review,” *J. Power Sources*, vol. 468, 2020, Art. no. 228376.
- [3] H. Yuan, H. Dai, X. Wei, and P. Ming, “A novel model-based internal state observer of a fuel cell system for electric vehicles using improved Kalman filter approach,” *Appl. Energy*, vol. 268, 2020, Art. no. 115009.
- [4] F. Nandjou, J. philippe Poirot-crouvezier, M. Chandresris, J. F. Blachot, C. Bonnaud, and Y. Bultel, “Impact of heat and water management on proton exchange membrane fuel cells degradation in automotive application,” *J. Power Sources*, vol. 326, pp. 182–192, 2016.
- [5] Z. Tang *et al.*, “Recent progress in the use of electrochemical impedance spectroscopy for the measurement, monitoring, diagnosis and optimization of proton exchange membrane fuel cell performance,” *J. Power Sources*, vol. 468, 2020, Art. no. 228361.
- [6] A. Sorrentino, K. Sundmacher, and T. Vidaković-Koch, “Polymer electrolyte fuel cell degradation mechanisms and their diagnosis by frequency response analysis methods: A review,” *Energies*, vol. 13, 2020, Art. no. 5825.
- [7] M. Heinzmann, A. Weber, and E. Ivers-Tiffée, “Advanced impedance study of polymer electrolyte membrane single cells by means of distribution of relaxation times,” *J. Power Sources*, vol. 402, pp. 24–33, 2018.
- [8] A. M. Dhirde, N. Dale, H. Salehfar, M. D. Mann, and T. Han, “Equivalent electric circuit modeling and performance analysis of a pem fuel cell stack using impedance spectroscopy,” *IEEE Trans. Energy Convers.*, vol. 25, no. 3, pp. 778–786, Sep. 2010.
- [9] H. Yuan, H. Dai, P. Ming, W. Xueyuan, and X. Wei, “Quantitative analysis of internal polarization dynamics for polymer electrolyte membrane fuel cell by distribution of relaxation times of impedance,” *Appl. Energy*, vol. 303, 2021, Art. no. 117640.
- [10] P. Ren *et al.*, “Diagnosis of water failures in proton exchange membrane fuel cell with zero-phase ohmic resistance and fixed-low-frequency impedance,” *Appl. Energy*, vol. 239, pp. 785–792, 2019.
- [11] A. Gebregergis, P. Pillay, and R. Rengaswamy, “PEMFC fault diagnosis, modeling, and mitigation,” in *Proc. IEEE Ind. Appl. Soc. Annu. Meeting*, 2008, pp. 1–8.
- [12] H. Yuan, H. Dai, X. Wei, and P. Ming, “Internal polarization process revelation of electrochemical impedance spectroscopy of proton exchange membrane fuel cell by an impedance dimension model and distribution of relaxation times,” *Chem. Eng. J.*, vol. 418, 2021, Art. no. 129358.

- [13] Q. Meyer and C. Zhao, "Air perturbation-induced low-frequency inductive electrochemical impedance arc in proton exchange membrane fuel cells," *J. Power Sources*, vol. 488, 2021, Art. no. 229245.
- [14] Q. Meyer, I. Pivac, F. Barbir, and C. Zhao, "Detection of oxygen starvation during carbon corrosion in proton exchange membrane fuel cells using low-frequency electrochemical impedance spectroscopy," *J. Power Sources*, vol. 470, 2020, Art. no. 228285.
- [15] I. Halvorsen, I. Pivac, D. Bezmalinović, F. Barbir, and F. Zenith, "Electrochemical low-frequency impedance spectroscopy algorithm for diagnostics of pem fuel cell degradation," *Int. J. Hydrogen Energy*, vol. 45, pp. 1325–1334, 2020.
- [16] R. Du, X. Wang, H. Dai, X. Wei, and P. Ming, "Online impedance spectrum measurement of fuel cells based on Morlet wavelet transform," *Int. J. Hydrogen Energy*, vol. 46, pp. 24339–24352, 2021.
- [17] C. Jeppesen, S. S. Araya, S. L. Sahlin, S. J. Andreasen, and S. K. Kær, "An EIS alternative for impedance measurement of a high temperature PEM fuel cell stack based on current pulse injection," *Int. J. Hydrogen Energy*, vol. 42, pp. 15851–15860, 2017.
- [18] D. Ritzberger, M. Striednig, C. Simon, C. Hametner, and S. Jakubek, "Online estimation of the electrochemical impedance of polymer electrolyte membrane fuel cells using broad-band current excitation," *J. Power Sources*, vol. 405, pp. 150–161, 2018.
- [19] S. Cruz-Manzo and P. Greenwood, "Study of oxygen diffusion in the cathode catalyst layer and gas diffusion layer for polymer electrolyte fuel cells with EIS," *J. Electroanalytical Chem.*, vol. 892, 2021, Art. no. 115270.
- [20] T. Hasegawa, H. T. shi Imanishi, M. Nada, and Y. Ikogi, "Development of the fuel cell system in the mirai FCV," SAE Int. Paper, Tech. Paper No. 2016-01-1185, 2016.
- [21] P. Hong, L. Xu, H. Jiang, J. Li, and M. Ouyang, "A new approach to online AC impedance measurement at high frequency of PEM fuel cell stack," *Int. J. Hydrogen Energy*, vol. 42, pp. 19156–19169, 2017.
- [22] X. Wang, X. Wei, Q. J. Chen, and H. Dai, "A novel system for measuring alternating current impedance spectra of series-connected lithium-ion batteries with a high-power dual active bridge converter and distributed sampling units," *IEEE Trans. Ind. Electron.*, vol. 68, no. 8, pp. 7380–7390, Aug. 2021.
- [23] X. Wang *et al.*, "A review of modeling, acquisition, and application of Lithium-ion battery impedance for onboard battery management," *eTransportation*, vol. 7, 2021, Art. no. 100093.
- [24] H. Lu, J. Chen, C. Yan, and H. Liu, "On-line fault diagnosis for proton exchange membrane fuel cells based on a fast electrochemical impedance spectroscopy measurement," *J. Power Sources*, vol. 430, pp. 233–243, 2019.
- [25] B. Bullecks, R. Suresh, and R. Rengaswamy, "Rapid impedance measurement using chirp signals for electrochemical system analysis," *Comput. Chem. Eng.*, vol. 106, pp. 421–436, 2017.
- [26] N. Katayama and S. Kogoshi, "Real-time electrochemical impedance diagnosis for fuel cells using a DC-DC converter," *IEEE Trans. Energy Convers.*, vol. 30, no. 2, pp. 707–713, Jun. 2015.
- [27] Y. Hoshi, N. Yakabe, K. Isobe, T. Saito, I. Shitanda, and M. Itagaki, "Wavelet transformation to determine impedance spectra of lithium-ion rechargeable battery," *J. Power Sources*, vol. 315, pp. 351–358, 2016.
- [28] M. Rubio, K. Bethune, A. Urquia, and J. St-Pierre, "Proton exchange membrane fuel cell failure mode early diagnosis with wavelet analysis of electrochemical noise," *Int. J. Hydrogen Energy*, vol. 41, no. 33, pp. 14991–15001, 2016.
- [29] A. Debenjak, P. Boskoski, B. Musizza, J. Petrovcic, and D. Juricic, "Fast measurement of proton exchange membrane fuel cell impedance based on pseudo-random binary sequence perturbation signals and continuous wavelet transform," *J. Power Sources*, vol. 254, pp. 112–118, 2014.
- [30] J. Jin, Z. Su, Y. Wei, and S. Lin, "Online estimation of membrane water content in vehicular PEMFC by complex morlet wavelet transformations," *SAE Int. J. Adv. Curr. Pract. Mobility*, vol. 3, no. 2020–01–2255, pp. 598–603, 2020.
- [31] R. G. Stockwell, L. Mansinha, and R. P. Lowe, "Localization of the complex spectrum: The S-transform," *IEEE Trans. Signal Process.*, vol. 44, no. 4, pp. 998–1001, Apr. 1996.
- [32] J. Xie, C. Wang, W. Zhu, and H. Yuan, "A multi-stage fault diagnosis method for proton exchange membrane fuel cell based on support vector machine with binary tree," *Energies*, vol. 14, no. 20, 2021, Art. no. 6526.
- [33] H. Yuan, H. Dai, P. Ming, L. Zhao, W. Tang, and X. Wei, "Understanding dynamic behavior of proton exchange membrane fuel cell in the view of internal dynamics based on impedance," *Chem. Eng. J.*, vol. 431, 2022, Art. no. 134035.



Hao Yuan received the B.E. degree in automotive engineering from Chongqing University, Chongqing, China, in 2017. He is currently working toward the Ph.D. degree in dynamic analysis and internal state identification of fuel cells based on electrochemical impedance with the Clean Energy Automotive Engineering Center, Tongji University, Shanghai, China.

His research interests include modeling, control, and diagnosis for fuel cell systems.



Runben Du received the Ph.D. degree in automotive engineering from Tongji University, Shanghai, China, in 2021.

He is currently working with Pan Asia Technical Automotive Center Company, Ltd., Shanghai. His research interests in modeling, diagnostics, and optimization for battery management system.



Xueyuan Wang was born in Anhui province, China, in 1990. He received the B.S. and Ph.D. degrees in automotive engineering from Tongji University, Shanghai, China, in 2014 and 2019, respectively.

He is currently a Postdoc with the Department of Control Science and Engineering, Tongji University. His research interests include modeling, acquisition, and applications of lithium-ion battery and fuel cell impedance.



Xuezhe Wei received the B.S. and M.S. degrees in electrical engineering and the Ph.D. degree in automotive engineering from Tongji University, Shanghai, China, in 1994, 1997, and 2005 respectively.

He is currently a Professor with the School of Automotive Studies, Tongji University. His research interests include battery system management, fuel cell system control, as well as electrical power conversion for electric vehicles.



Haifeng Dai (Senior Member, IEEE) received the B.S. and M.S. degrees in mechanical engineering and the Ph.D. degree in automotive engineering from Tongji University, Shanghai, China, in 2003, 2005, and 2008, respectively.

He is currently a Professor with the School of Automotive Studies, Tongji University. His research interests include battery system management, fuel cell system control, as well as electrical power conversion for electric vehicles.